AIAA JOURNAL
Vol. 45, No. 10, October 2007

Numerical Simulation of a Flapping Foil with Chordwise or Spanwise Flexibility

Qiang Zhu*
University of California, San Diego, La Jolla, California 92093-0085

DOI: 10.2514/1.28565

Motivated by the discovery that living creatures may be able to enhance their locomotion capability through passive or active deformations of their wings or fins, we carry out a fully coupled fluid–structure interaction study to investigate the flapping motion of a foil with either chordwise or spanwise flexibility. We employ a fluid–structure interaction model, which accounts for fluid dynamics using the boundary-element method and structural dynamics using a two-dimensional nonlinear thin-plate model. With this approach, we numerically investigate the effect of structural deformation on the performance of the foil when it is immersed in two different fluids, a low-density fluid (e.g., air), in which the deformation is determined primarily by the inertia of the foil, and a high-density fluid (e.g., water), in which the fluid loading has a significant impact. In the first scenario, we find that the chordwise flexibility reduces both the thrust and the propulsion efficiency and the spanwise flexibility increases the thrust without efficiency reduction within a small range of structural parameters. In the second scenario, we find that the chordwise flexibility increases the efficiency. The spanwise flexibility, on the other hand, compromises the performance of the foil by diminishing both the thrust and the efficiency. Possible applications of these findings and their relation to designs in aquatic animals are discussed.

Nomenclature

c	=	chord length of the foil
D	=	hysteretic damping coefficient
d	=	thickness of the foil
E	=	Young's modulus of the foil
$\bar{F}$	=	mean thrust force in the direction of U
$\boldsymbol{F}_h$	=	hydrodynamic load per unit length
h	=	heave motion
h_0	=	amplitude of heave
l	=	span length of the foil
S_b	=	body surface
S_t	=	Strouhal number, $\omega h_0/\pi U$
S_w	=	wake sheet
t	=	time
U	=	forward speed
x, y, z	=	Cartesian coordinates
η	=	propulsion efficiency
θ	=	pitch motion
θ_0	=	amplitude of pitch
ρ	=	density of fluid
ρ_b	=	density of the foil
Φ	=	velocity potential
ϕ_b	=	velocity potential caused by the body
ϕ_w	=	velocity potential caused by the wake
φ	=	phase between heave and pitch
ω	=	frequency of oscillation

I. Introduction

As a novel biomimetic technology, flapping foils have attracted much attention, owing to their capacity of producing thrust with high efficiency [1–3]. During its unsteady motion, a flapping foil is also capable of producing large transient force that is useful in maneuvering and motion stabilization [4]. With these two characteristics, flapping foils may find applications on autonomous underwater vehicles working under complex conditions when both high propulsion efficiency and large instantaneous force generation are required.

Unlike their prototypes in nature (i.e., wings and fins of aquatic or airborne animals, which allow large bending, twisting, and other deformations), artificial flapping foils are usually designed to be rigid to avoid strong structural interaction with the flowfield. Indeed, fluid–structure interactions are often considered hazardous in engineering, as manifested in examples such as vortex-induced vibrations and galloping of flexible architectural/offshore structures. In these cases, the fluid–structure interactions compromise the stability and performance of the structures, reduce structural integrity, and even cause safety concerns. Much effort has been expended to mitigate these hazardous fluid–structure interactions (e.g., see Jones and Platzer [5]).

Using novel computational and experimental tools, recent biomechanics studies have brought a new understanding about the role of fluid–structure interaction, depicting it as a potential measure for performance enhancement in biolocomotion. For example, morphological research of insect wings suggests that through specific arrangement of supporting veins, these wings appear to allow certain passive deformations that benefit the production of lifting and thrusting forces, whereas deformations that are detrimental to the aerodynamic performance are discouraged [6–8]. Similar phenomena are also found in the aquatic environment. By examining the swimming of a fish within a vorticity field, Liao et al. [9] demonstrated that a flexible body was able to extract energy from the incoming vortices and generate thrust. Zhang et al. [10] studied the motion of a flexible filament in a flowing soap flow and observed that via passive deformations, the filament performed a wavelike undulation, resembling the locomotive motion of aquatic creatures.

The beneficial role of fluid–structure interactions has also been discovered through studies in flapping-foil propulsion. By studying the performance of a flapping foil with the front part rigid and the rear part flexible, Yamamoto et al. [11] reported as much as a 27% increase in propulsion efficiency compared with a rigid foil. Through examining the oscillation of a two-dimensional plate, Katz and Weihs [12,13] were able to demonstrate that a certain amount of chordwise flexibility could increase the efficiency by 20%. Spanwise deformations, on the other hand, were found to decrease the performance of the foil, unless some form of active control was applied [14]. In this work, however, instead of solving the coupled

Received 26 October 2006; revision received 1 May 2007; accepted for publication 4 June 2007.

*Assistant Professor, Department of Structural Engineering; qizhu@ucsd.edu.

fluid–structure interaction problem, the foil deformations were prescribed. Indeed, the existing numerical/analytical studies often neglect the three-dimensional effects, nonlinear structural responses, and fully coupled fluid–structure interactions. In particular, the foil deformation is assumed to be caused completely by fluid forcing, whereas the inertia and the structural dissipation of the foil are ignored. Such assumptions are not always valid. Inertia has been found to play a vital role in the structural dynamics of flapping foils. For instance, by studying the shape change of insect wings during flying, Daniel and Combes [15] concluded that due to the low density of the air, the deformations were determined primarily by the inertia of the wings. Inertia has a dual effect on the overall dynamics of a flapping foil. First, it influences the foil deformation. Compared with a foil with finite mass, a zero-inertia foil deforms under the instantaneous fluid loads and therefore it has no memory effect. Second, inertia also interferes with the process of energy exchange between the fluid and the structure. This comprehensive energy-exchange process is not included in previous works, owing to the absence of the inertia effect.

The primary purpose of the present work is to investigate a fully coupled flapping-foil problem in which the deformation of the foil is determined vis-à-vis the fluid loads, the inertia, the structural elasticity, and the external actuation forces/moments. We develop a nonlinear fluid–structure interaction approach to study the unsteady oscillation of a flexible foil. This hybrid approach includes a three-dimensional boundary-integral method to solve the flow around the body and the dynamics of the wake and a nonlinear thin-plate model to simulate the structural response of the foil. For simplicity, we examine cases with only two-dimensional structural responses (i.e., the foil can only be bent in either the chordwise direction or the spanwise direction), although the surrounding fluid flow is essentially three-dimensional. To clarify the role of inertia on the deformation of the foil, we study the motion of a foil in both air and water. In the first case, we find that the deformation of the foil during the oscillation is indistinguishable from the results obtained by neglecting the fluid forcing. This indicates that the inertia of the foil should be the dominant factor in determining the structural deformation. In the second case, to the contrary, we find that the deformation is significantly affected by the fluid loads.

The rest of the paper is organized as follows. In Sec. II, we describe the physical problem of a flexible foil undergoing translation and periodic heaving/pitching motion. Section III presents the mathematical formulations and the numerical method. The numerical results are presented in Sec. IV, followed by the Conclusions in Sec. V.

II. Problem Description

As shown in Fig. 1, we consider the unsteady motion of a three-dimensional rectangular foil with chord c and span l. The foil has a uniform thickness, except for the smoothly tapered leading edge and the sharp trailing edge. In a space-fixed Cartesian frame (x, y, z), the foil moves in the $-x$ direction with constant speed U. In addition, it also undergoes prescribed heaving and pitching motions. The heaving motion $h = h_0 \sin \omega t$ occurs in the z direction. The pitching motion $\theta = \theta_0 \sin(\omega t + \varphi)$ is around an axis at the front edge.

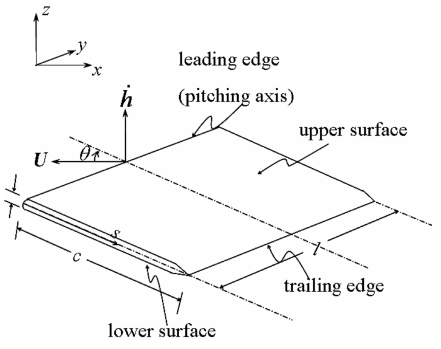

Fig. 1 The heaving/pitching motion of a foil undergoing translation.

In general, a foil made of flexible materials is able to be bent and twisted in all directions. The present work, however, focuses on two simple cases: a foil that can only be bent along its chord (chordwise flexibility) and a foil that can only be bent along the span (spanwise flexibility). In both cases, the structural dynamics is essentially two-dimensional.

In the chordwise-flexibility case, we assume that the motion at the leading (front) edge is prescribed as the heave/pitch combination. The rest of the foil follows this motion passively. There is neither strain nor bending moment at the trailing edge. In the spanwise-flexibility case, the midspan of the foil performs the predescribed heaving/pitching motion, and the tips of the foil are described as free ends without strain/bending.

III. Mathematical Formulations and Numerical Methods

To investigate the fluid–structure interactions, we must take into account two interconnected problems simultaneously. One of them is the fluid flow around the foil and the other is the structural response of the body. These two problems are coupled through the fluid-induced structural deformations and the subsequent nonlinear variation of the body boundary condition.

A. Structural Dynamics of the Foil

We first consider the nonlinear structural response of a foil with chordwise flexibility. Mathematically, the problem is modeled as the nonlinear motion of a two-dimensional thin plate with uniform thickness d and Young's modulus E (for simplicity, the tapering at the leading and trailing edges is neglected in the structural model). The motion of the leading edge is prespecified and the trailing edge is free, with zero stretching and bending.

The instantaneous configuration of the thin foil undergoing translational, oscillating, and deformational motions is denoted by the instantaneous location of its centerline. It is convenient to define an additional Lagrangian coordinate s, which measures the unstretched distance from any point on the centerline of plate to the end with prescribed motion (in this case, the leading edge). Let $\boldsymbol{x}_p(s, t) = (x_p, z_p)$ be the x and z location of any point along the centerline of the foil. By using the thin-plate assumption ($d \ll c$), the potential energy of the foil is given as (e.g., see Doyle [16])

$$V = \frac{1}{2} E \int_0^c \left\{ \mathrm{d} \left[\left(\frac{\partial \boldsymbol{x}_p}{\partial s} \cdot \frac{\partial \boldsymbol{x}_p}{\partial s} \right)^{1/2} - 1 \right]^2 + \frac{\mathrm{d}^3}{12} \left(\frac{\partial^2 x_p}{\partial s^2} \cdot \frac{\partial^2 x_p}{\partial s^2} \right) \right\} \mathrm{d}s \tag{1}$$

Similarly, the kinetic energy is

$$T = \frac{1}{2} \int_0^c \rho_b \, \mathrm{d} \frac{\partial \boldsymbol{x}_p}{\partial t} \cdot \frac{\partial \boldsymbol{x}_p}{\partial t} \, \mathrm{d}s \tag{2}$$

where E is Young's modulus, and ρ_b is the density of the foil. Employing variational analysis, within any time interval (t_1, t_2), we have

$$\int_{t_1}^{t_2} \mathrm{d}t \left[\delta(T - V) + \int_0^c \boldsymbol{F}_h \cdot \boldsymbol{x}_p \, \mathrm{d}s \right] = 0 \tag{3}$$

where $\boldsymbol{F}_h$ is the hydrodynamic loading per unit chord length on the foil, which is obtained by evaluating the pressure difference between the upper and lower surface of the foil:

$$\boldsymbol{F}_h(s, t) = \overline{p_u \boldsymbol{n}_u + p_l \boldsymbol{n}_l} \tag{4}$$

where p_u and p_l are the hydrodynamic pressure on the upper and lower surfaces of the foil, and n_u and n_l are the unit normal vectors pointing into the foil on the upper and lower surfaces, respectively. The average is evaluated over the span of the foil.

By substituting Eqs. (1) and (2) into Eq. (3) and considering the fact that the equation is valid at arbitrary t_1 and t_2, we have

$$\rho_b h \frac{\partial^2 \boldsymbol{x}_p}{\partial t^2} + \frac{Ed^3}{12}\frac{\partial^4 \boldsymbol{x}_p}{\partial s^4} - Ed\frac{\partial}{\partial s}\left\{\left[1 - \left(\frac{\partial \boldsymbol{x}_p}{\partial s}\cdot\frac{\partial \boldsymbol{x}_p}{\partial s}\right)^{-1/2}\right]\frac{\partial \boldsymbol{x}_p}{\partial s}\right\} = \boldsymbol{F_h}, \quad \boldsymbol{0} < s < c \tag{5}$$

In Eq. (5), the first term on the left-hand side represents the inertia effect; the second and third terms depict the elastic effects of bending and stretching, respectively; and the right-hand-side term stands for the external driving force imposed by the fluid load.

To model the hysteretic damping caused by internal friction, we replace Young's modulus E in Eq. (5) by $E(1 + D\partial/\partial t)$, where D denotes the magnitude of the energy dissipation.

At the leading edge with prescribed motion ($s = 0$), we have

$$\boldsymbol{x}_p(0, t) = \boldsymbol{x}_p(0, 0) + [-Ut, h(t)]^T \tag{6}$$

and

$$\frac{\partial \boldsymbol{x}_p(0, t)}{\partial s} = [\cos\theta(t), -\sin\theta(t)]^T \tag{7}$$

At the trailing edge ($s = c$), we have the stress-free condition

$$-Eh\left[1 - \left(\frac{\partial \boldsymbol{x}_p}{\partial s}\cdot\frac{\partial \boldsymbol{x}_p}{\partial s}\right)^{-1/2}\right]\frac{\partial \boldsymbol{x}_p}{\partial s} + \frac{Eh^3}{12}\frac{\partial^3 \boldsymbol{x}_p}{\partial s^3} = 0 \tag{8}$$

and the zero-bending condition

$$\frac{\partial^2 \boldsymbol{x}_p}{\partial s^2} = 0 \tag{9}$$

The formulation of a foil with spanwise flexibility is similar to that of a foil with chordwise flexibility, described earlier. Because of the symmetry, we only need to consider half of the span: $0 \le s \le l/2$ (here, the Lagrangian coordinate s is defined to be the unstretched distance to the midspan of the foil).

B. Modeling of Fluid Flow Around the Foil

We assume that the flow around the foil is irrotational, except for an infinitesimally thin wake shed from the trailing edge of the foil, which is modeled as a shear layer. Following Zhu et al. [17], we write the flow potential $\Phi(\boldsymbol{x}, t)$ as the linear superposition of two parts: $\Phi = \phi_b + \phi_w$, where ϕ_b represents the contribution from the foil body and ϕ_w is the contribution from the wake. With this decomposition, at any instant, there are two interdependent problems: the boundary-value problem for ϕ_b and the generation/evolution of the wake, which determines ϕ_w.

The boundary-value problem for ϕ_b consists of the Laplace equation $\nabla^2\phi_b = 0$ inside the fluid domain, a far-field condition imposed at a large distance from the body (so that the influence of the body vanishes there) and a Neumann condition on the foil surface S_b:

$$\boldsymbol{n}\cdot\nabla\phi_b = \boldsymbol{n}\cdot[\boldsymbol{V}_b(\boldsymbol{x}, t) - \nabla\phi_w] \tag{10}$$

where $\boldsymbol{V}_b$ is the instantaneous velocity of the foil, and $\boldsymbol{n}$ is the unit normal vector pointing into the body.

Invoking Green's theorem, at any point $\boldsymbol{x} = (x, y, z)$ on the foil surface ($\boldsymbol{x} \in S_b$), we have

$$2\pi\phi_b(\boldsymbol{x}, t) + \iint_{S_b}\phi_b(\boldsymbol{x}', t)\boldsymbol{n}\cdot\nabla(1/|\boldsymbol{x} - \boldsymbol{x}'|)\,\mathrm{d}s' = \iint_{S_b}(1/|\boldsymbol{x} - \boldsymbol{x}'|)\boldsymbol{n}\cdot\nabla\phi_b(\boldsymbol{x}', t)\,\mathrm{d}s' \tag{11}$$

where $\boldsymbol{n}\cdot\nabla\phi_b$ is given by using Eq. (10), and the body influence potential ϕ_b at the foil surface S_b is evaluated by solving Eq. (11). Subsequently, the value of ϕ_b at any point $\boldsymbol{x}$ inside the fluid is

$$\phi_b(\boldsymbol{x}, t) = -\frac{1}{4\pi}\iint_{S_b}\phi_b(\boldsymbol{x}', t)\boldsymbol{n}\cdot\nabla[1/(\boldsymbol{x} - \boldsymbol{x}')]\,\mathrm{d}s' + \frac{1}{4\pi}\iint_{S_b}[1/(\boldsymbol{x} - \boldsymbol{x}')]\boldsymbol{n}\cdot\nabla\phi_b(\boldsymbol{x}', t)\,\mathrm{d}s' \tag{12}$$

We note that Eq. (10) involves the wake influence potential ϕ_w, which has to be predetermined. To achieve this, we simulate this wake using a distribution of dipoles on the wake sheet originated from the sharp trailing edge of the foil. A new portion of the wake is created at every time step, representing the continuous shedding of vortices from the trailing edge. The strength of the newly shed wake is determined by the explicit Kutta condition [17,18]; that is, the new wake strength ϕ_w at the trailing edge equals the instantaneous difference of body influence potential ϕ_b between the upper and lower surfaces near the edge. The implicit Kutta condition, which enforces a zero-pressure-difference condition across the trailing edge through Newton–Raphson iterations [19], is generally a more accurate physical description. It is, however, computationally expensive, owing to the evaluation of the Jacobian, and so it is not used in the current study.

The rest of the wake, treated as a material surface, is carried downstream by the collective effect of the upcoming flow and the self-induced velocity. Meanwhile, its strength is kept unchangeable, due to the absence of dissipation (refer to Zhu et al. [17] or Zhu et al. [20] for a detailed description).

C. Hydrodynamic Pressure and Force

With the flow potential Φ determined by summing up the body influence potential ϕ_b and the wake influence potential ϕ_w, the hydrodynamic pressure distribution on the body surface is readily obtained via Bernoulli's equation:

$$p(x, t) = -\rho\left(\frac{\partial\Phi}{\partial t} + \frac{1}{2}\nabla\Phi\cdot\nabla\Phi\right) \tag{13}$$

where ρ is the density of the fluid. Integration of this pressure over the foil surface yields the total hydrodynamic force $\boldsymbol{F}$:

$$\boldsymbol{F}(t) = \oiint_{S_b} p\boldsymbol{n}'\,\mathrm{d}s' \tag{14}$$

Similarly, the rate of energy input P, which is by definition the power required to move the body, is given as

$$P(t) = \oiint_{S_b} p\boldsymbol{V}_b\cdot\boldsymbol{n}'\,\mathrm{d}s' \tag{15}$$

Finally, the mean propulsive efficiency, an important factor of the foil performance, is defined as

$$\eta = U\bar{F}/\bar{P} \tag{16}$$

where U is the forward speed, $\bar{F}$ is the mean hydrodynamic force in the direction of U, and $\bar{P}$ is the mean energy input.

D. Numerical Methods

1. *Boundary-Element Method*

We solve the fluid dynamic problem for the flow potential Φ with a low-order boundary-element algorithm (e.g., see Katz and Plotkin [21]). In this approach, the foil surface S_b is discretized into N_b quadruple panels S_{bj} ($j = 1, \ldots, N_b$). The number of panels across the span is N_{bs} (evenly distributed), and N_{bc} panels are employed along the chord, following a cosine distribution with high panel density near the leading and the trailing edges. In addition, N_{bc} panels are added at each tip to close the gap, bringing the total number of panels to be $N_b = N_{bs}\cdot N_{bc} + 2N_{bc}$. Within each panel, the body potential ϕ_b and its normal derivative are assumed to be constants. By collocating at the centroids of the panels, Eq. (10) becomes a system

of N_b linear equations with N_b unknowns and can be readily solved through numerical means.

Similarly, the wake sheet is also segmented into N_w elements, and within each panel, the dipole strength is assumed to be a constant. At each time step, new panels are created at the trailing edge, their strengths determined through the Kutta condition. Consequently, N_w increases with time. The distribution of the body and wake panels is illustrated in Fig. 2.

The discretely distributed vorticity used in the current model is susceptible to instabilities. To stabilize the computation, it is necessary to introduce a desingularization algorithm [22] by assigning a finite core radius δ to each (body or wake) panel of dipole distribution. The induced velocity at any point by the dipoles in this panel will then be evaluated through the desingularized Biot–Savart law:

$$\boldsymbol{V}(x) = \frac{\Gamma}{4\pi}\oint \frac{\boldsymbol{s}\times\boldsymbol{r}}{r^3+\delta^3}\,\mathrm{d}l \tag{17}$$

where Γ is the circulation of the vortex ring around the sides of the panel (which is equivalent to a uniform distribution of normal dipoles inside the panel), $\boldsymbol{s}$ is the tangent vector of the panel, $\boldsymbol{r}$ is the vector from the integration element to the field point $r = |\boldsymbol{r}|$, and the path of integration is along the four sides of the panel. The inclusion of the desingularization factor effectively prevents the ill-posed dynamical problem associated with zero-thickness shear layers and stabilizes wake evolution.

2. Simulation of Structural Deformation

To obtain the instantaneous deformation of the foil, we solve the differential Eq. (5) and boundary conditions (6–9) via a finite difference approach. Considering the chordwise-flexible foil, we use N_d evenly distributed grids s_j ($j = 1, \ldots, N_d$) along the centerline of the chord. Let f represent x_d, z_d, or any of their combinations, and let $f_j^n = f(s_j, n\Delta t_s)$. Equations (5–9) are discretized by rewriting the derivatives as

$$\frac{\partial^2 f}{\partial t^2} = \frac{f_j^{n+1} - 2f_j^n + f_j^{n-1}}{\Delta t_s^2} \tag{18}$$

$$\frac{\partial f}{\partial s} = \frac{f_{j+1}^{n+1} - f_{j-1}^{n+1}}{2\Delta s} \tag{19}$$

$$\frac{\partial^3 f}{\partial s^3} = \frac{-5f_j^{n+1} + 18f_{j+1}^{n+1} - 24f_{j+2}^{n+1} + 14f_{j+3}^{n+1} - 3f_{j+4}^{n+1}}{2\Delta s^3} \quad \text{or}$$
$$\frac{\partial^3 f}{\partial s^3} = \frac{5f_j^{n+1} - 18f_{j-1}^{n+1} + 24f_{j-2}^{n+1} - 14f_{j-3}^{n+1} + 3f_{j-4}^{n+1}}{2\Delta s^3} \tag{20}$$

$$\frac{\partial^4 f}{\partial s^4} = \frac{f_{j+2}^{n+1} - 4f_{j+1}^{n+1} + 6f_j^{n+1} - 4f_{j-1}^{n+1} + f_{j-2}^{n+1}}{\Delta s^4} \tag{21}$$

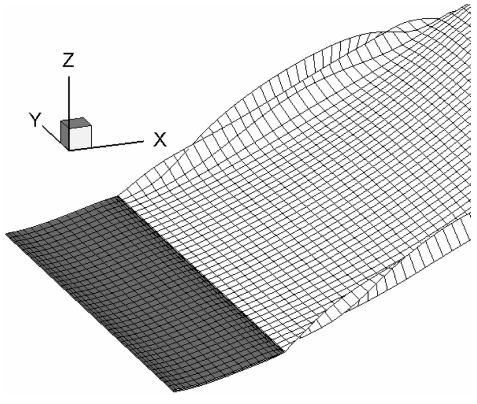

Fig. 2 Distribution of body and wake panels.

where Δt_s is the time step for structural calculation, and Δs is the size of each grid. The resulting system of nonlinear equations is solved by a Newtonian iteration scheme.

3. Coupling of Fluid–Structure Solvers

The fluid dynamic equations and the structural responses need to be solved simultaneously. For numerical stability, integration of the structural dynamics [Eq. (5)] usually requires a much smaller time step than that applied in the fluid simulations. An iteration algorithm is thus developed so that the two coupled problems are resolved separately within an iteration loop, which corresponds to one time step Δt in fluid dynamics calculation and to N_t time steps in structural simulation ($\Delta t = N_t \Delta t_s$). In the current study, we choose $N_t \sim O(10^2)$ to guarantee stability of the structural solver. The primary steps of the iteration are outlined next:

Step 1) At any time t, we start from an initial guess that the deformation of the foil remains the same as the previous time step $t - \Delta t$.

Step 2) The hydrodynamic problem is solved based on the updated heave $h(t)$, the updated pitch angle $\theta(t)$, and the guessed deformation to evaluate the hydrodynamic forcing.

Step 3) Equation (5), which governs the structural response of the foil, is numerically integrated using N_t time steps to obtain the updated deformation.

Step 4) If the updated deformation is not sufficiently close to the guessed deformation, we set it to be our new guess and repeat steps 2–4.

A linear interpolation scheme is applied to determine the location of surface panels based on the instantaneous shape of the centerline obtained in the structural simulation. In all cases, we find that only a few iteration loops are requested to achieve high-precision convergence.

E. Convergence Tests

To test the sensitivity of our hybrid scheme with respect to numerical parameters, we perform convergence tests by considering the heave-only motion of a foil in water and with $S_t = 0.20$. The foil has a rectangular shape with $c = 0.1$ m, $l/c = 4$, and $d/c = 0.01$. Its density is $\rho_b = 10^3$ kg/m^3. Its Young's modulus is $E/\rho_b g c = 10^5$, and the hysteretic damping coefficient is $D = 0.1$ s. Table 1 shows the propulsion efficiency η as a function of N_{bs} and N_{bc}, obtained with the time step $\Delta t = T/64$ ($T = 2\pi/\omega$ is the period of motion), $N_d = 30$, and $N_t = 200$.

The convergence with respect to both parameters is clearly displayed in Table 1. Although the method is a low-order approach with respect to body panel size, for reasonably large number of body panels, an accuracy of ~4% is achieved, which is adequate for most practical applications. Similarly, Table 2 demonstrates the convergence of η with respect to the time step Δt when $N_{bs} = N_{bc} = 40$.

Additional tests were conducted to examine the influence of N_d [the number of grids applied to calculate the deformation of the foil based on Eq. (5)], N_t (the ratio between the time step used in the fluid

Table 1 Convergence of the propulsion efficiency with respect to the number of panels on the foil surface

N_{bs}/N_{bc}	10	20	40	80
10	0.274	0.537	0.738	0.767
20	0.270	0.532	0.732	0.760
40	0.269	0.529	0.729	0.757

Table 2 Convergence of the propulsion efficiency with respect to the time step

$T/\Delta t$	32	64	128	256
η	0.706	0.729	0.742	0.749

dynamics computation and that in the structural mechanics computation), and δ (the desingularization factor). Within reasonable ranges of these parameters [i.e., $N_d > 20$, $N_t \sim O(10^2)$, and $\delta/c \in (0.001, 0.1)$], no significant variations are recorded.

Based upon these tests, we select the following numerical parameters in the calculations described in Sec. IV: $N_{bs} = N_{bc} = 40$, $\Delta t = T/64$, $N_d = 30$, $N_t = 200$, and $\delta/c = 0.01$.

F. Comparison with Existing Works

Although the method has been proven to be convergent through the preceding tests, it is necessary to keep in mind that the formulation is based upon the assumption that no flow separation is possible until at the sharp trailing edge. This assumption has been demonstrated to be valid only within a limited range of kinetic parameters. According to a visualization of the near-body flowfield around a flapping foil [3], a significant amount of vorticity is generated near the leading edge when Strouhal numbers are large. In the same study, it was shown that when $S_t > 0.3$, the occurrence of leading-edge separation causes significant discrepancies between experimental measurements and inviscid model predictions.

To further prove the validity of the current methodology and to determine the region of kinetic parameters within which the accuracy of this method is guaranteed, we herein compare our numerical predictions using both the standalone boundary-element method and the coupled BEM-structure method to benchmark results of flapping foils obtained through experiments and fully viscous Navier–Stokes (N–S) simulations.

In Fig. 3, we plot the BEM predictions of the thrust coefficient of a NACA0012 foil undergoing periodic plunging motions, together with the two-dimensional results obtained by Tuncer and Platzer [23] using N–S equations. To mitigate the effect of three-dimensionality, our BEM simulations were performed with a slender foil with a span-to-chord ratio of 10. As is shown in the figure, an excellent match between the two methods is obtained until the Strouhal number (defined as $S_t = \omega h_0/\pi U$) reaches 0.13, at which point a discrepancy of 7% exists between the two predictions.

To demonstrate the performance of BEM at larger Strouhal numbers, in Fig. 4 we display the comparison between our BEM predictions and the experimental measurements conducted by Read [4] about the thrust generation of a NACA0012 foil with a span-to-chord ratio of 6 undergoing a prescribed heaving-pitching motion. The heaving amplitude is $0.75c$, and the pitching motion is lagged behind the heaving motion by 90 deg with the pitching axis located at a one-third-chord length from the leading edge. Figure 5 shows that our numerical results remain close to the experimental measurements up until $S_t = 0.3$, consistent with the predictions by Anderson et al. [3].

We also compared predictions of the coupled fluid–structure model with experimental measurements. In contrast to the abundance of benchmark results about rigid flapping foils, to date, there are few works about unsteady dynamics of flexible foils. One of these is the experiment performed by Heathcote et al. [24], who examined the propulsive force generated by a steel plate undergoing periodic heaving motion in still water. To match the experimental setup, in our numerical model, we use a foil with a span of 0.6 m and a chord of 0.09 m. Two different foil thickness, 4 mm (thick foil) and 1 mm (thin foil), are used. Young's modulus of the foil is chosen to be 200 GPa and the density is 7800 kg/m^3. The Reynolds number, defined as $2\pi\omega c^2/\nu$ (ν is the kinetic viscosity), is 2.025×10^4. The heaving amplitude is $h_0 = 0.192c$.

As we can see, in the experiment there is no upcoming stream and so the Strouhal number approaches infinity. Clearly, this is beyond the regime in which the BEM is accurate, and so its prediction of hydrodynamic forces (mean thrust, etc.) is not directly comparable with the experiment. Nevertheless, in Fig. 5, we display the deformation of the foil characterized by the relative position of the leading edge z_{LE} and the trailing edge z_{TE}. Interestingly, good comparison between the experiment and the model prediction is obtained. The implication is that the leading-edge separation does not play an important role in determining the foil deformation. Instead, the shape change is caused primarily by the added mass effect.

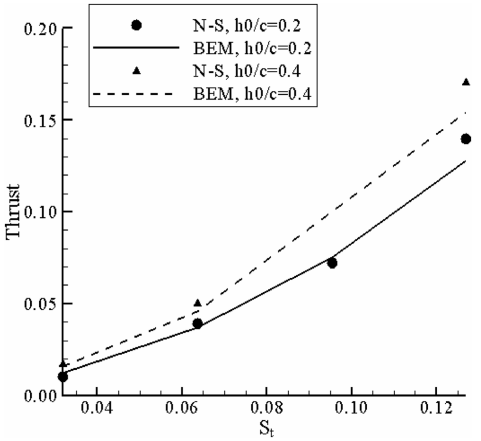

Fig. 3 Comparison between the mean thrust (normalized by $\frac{1}{2}\rho csU^2$) generated by a foil undergoing heave motion predicted by the N–S simulations by Tuncer and Platzer [23] at a Reynolds number of 3×10^6 and the boundary-element predictions.

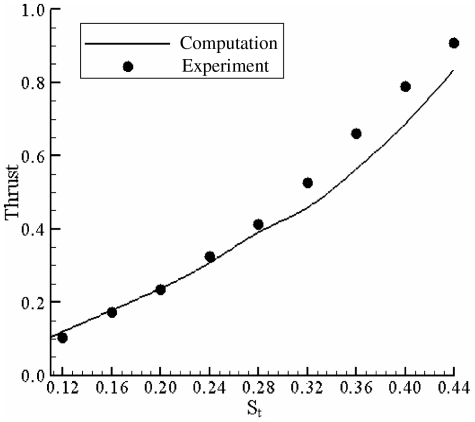

Fig. 4 Comparison between the experimental measurements in Read [4] at a Reynolds number of 4×10^4 and boundary-element predictions of the mean thrust (normalized by $\frac{1}{2}\rho csU^2$) generated by a foil undergoing heave and pitch motions. In both experiments and simulations, the maximum angle of attack is prescribed to be 20 deg.

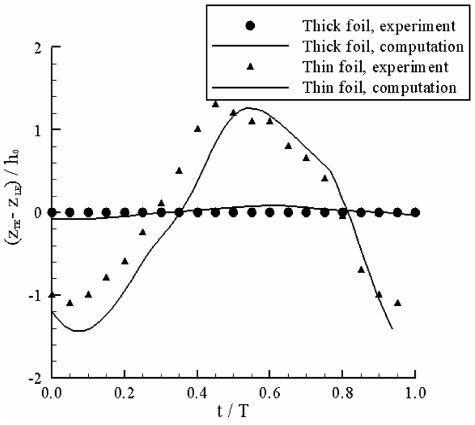

Fig. 5 Comparison between the experimental measurements by Heathcote et al. [24] and our fluid–structure interaction model prediction of the deformation of a steel plate undergoing periodic heaving motion.

IV. Results

To numerically examine the dynamics of a flapping foil, we study the same foil as that employed in the convergence tests. In all the testing cases, we use the forward speed $U = 0.4$ m/s and the heaving

amplitude $h_0 = c$. The phase difference between the heave and the pitch motions, φ, is chosen to be 90 deg. We study the foil in both air ($\rho = 1$ kg/m^3) and water ($\rho = 10^3$ kg/m^3) and compare the two results against each other. In the first scenario, our numerical results indicate that the deformation of the foil is almost identical to the case when there is no fluid force. We thus call it the inertia-driven deformation. The second scenario, on the other hand, displays considerable fluid–structure interaction features. It is subsequently called the fluid-driven deformation.

The Strouhal number plays a pivotal role in determining the efficiency of the flapping-foil system. Based upon the comparisons with benchmark N–S simulations and experiments, we have shown that the boundary-element method applied in our model is accurate up until $S_t \sim 0.3$, when the effect of leading-edge separation is insignificant. On the other hand, as illustrated by Triantafyllou et al. [25], the optimal propulsion efficiency of a flapping foil occurs at $S_t \sim 0.2$–0.3, corresponding to maximum development of the inverse Kármán vortex street within the wake. In the following simulations, to study the oscillating foil near its optimal performance and to avoid inaccuracy caused by leading-edge separation, we select $S_t = 0.2$.

We first investigate the heaving/pitching motion of a foil with chordwise flexibility. As shown in Fig. 6, we find that the inertia-driven deformation (corresponding to the foil in air) and the fluid-driven deformation (corresponding to the foil in water) have distinctively different characters. In the fluid-driven case, the foil is always bent toward the trajectory of the leading edge (feathering); that is, the hydrodynamic forces and moments cause the foil to bend toward the tangential direction of the flow velocity. Therefore, the foil appears to "follow" the ambient flow. This feature reminds us of the experiment done by Liao et al. [9], in which a dead fish was observed to maneuver itself between the incoming vortices in a Kármán vortex street.

The inertia-driven deformation, not surprisingly, does not show that flow-following tendency. Instead, the bending of the foil tends to send the trailing edge away from the track (most conspicuously, near the peaks or the troughs). Consequently, the heaving amplitude near the trailing edge is larger than the prescribed amplitude at the leading edge and it creates a wider wake. This is analogous to the simple vibrating system shown in Fig. 7 (left), which consists of two masses m_1 (corresponding to the leading edge with specified kinetics) and m_2 (corresponding to an arbitrary point along the chord) linked by a spring k and a dissipater μ. If m_1 is subjected to an imposed sinusoidal motion with frequency ω, the displacement transmissibility T_d, defined as the ratio between the amplitude of m_2 and the amplitude of m_1, is obtained as

$$T_d = \left\{ \frac{1 + (2b\omega/\omega_n)^2}{[1 - (\omega/\omega_n)^2]^2 + (2b\omega/\omega_n)^2} \right\}^{1/2} \tag{22}$$

where $\omega_n = \sqrt{k/m_2}$ and $b = \mu\omega_n/(2k)$. As plotted in Fig. 7 (right), we see that $T_d > 1$ as $\omega/\omega_n < \sqrt{2}$ when the motion of m_2 is larger than that of m_1 (amplification region), whereas $T_d < 1$ as $\omega/\omega_n > \sqrt{2}$ when the motion is not effectively transferred from m_1 to m_2 (isolation region).

Resembling this simple model, we also observe the motion amplification and the motion isolation in the present study of the flexible foil motion when the deformation is determined primarily by inertia (although in the cases with chordwise flexibility, the motion isolation does not appear, owing to the range of parameters). The amplification leads to a larger heaving amplitude on average and sometimes a thrust increase, whereas the isolation diminishes the average heaving amplitude and reduces the thrust.

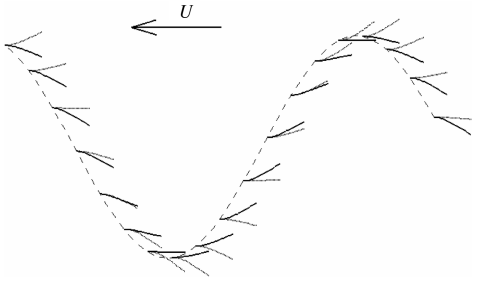

Fig. 6 Typical configurations of the center line of a foil flexible along the chord during heave with fluid-driven deformations (solid line) and inertia-driven deformations (dots). The trajectory of the front edge is shown in dashed line. The amplitude of pitch is zero.

A. Case 1: Fluid-Driven Deformation of a Chordwise-Flexible Foil

Figure 8 shows the performance of the foil with various stiffnesses in the fluid-driven case. It is seen that as Young's modulus is reduced, the propulsion efficiency rises. Indeed, an efficiency increase as large as 20% is observed. This, however, is at the cost of thrust reduction. This behavior proves that by carefully choosing the chordwise flexibility, it is possible to considerably increase the propulsion efficiency of the foil, especially in cases when the kinematic parameters are not optimized (for example, the case with zero pitch motion). This phenomenon is both qualitatively and quantitatively consistent with the experimental measurements by Yamamoto et al. [11], although the foil used in that experiment had three-dimensional flexibility, and with the finding by Katz and Weihs [12,13] using a two-dimensional analytical approach.

One explanation for the efficiency increase of the fluid-driven chordwise deformation was provided by Katz and Weihs [12]. By examining the instantaneous curvature of the foil, they concluded that while the foil is bent, the component in the hydrodynamic force toward the direction of motion (i.e., thrust) is increased. Indeed, a similar effect is observed in our study. As shown in Fig. 6, the foil curvature reaches its maximum value near $z = 0$, at which point the maximum thrust is recorded.

Our simulation also indicates another reason for efficiency enhancement. As discussed earlier, the fluid-driven deformation

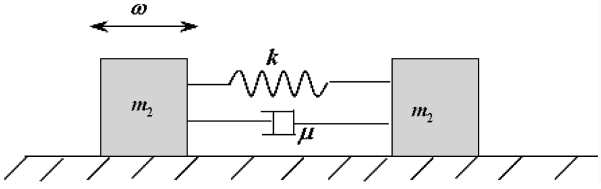

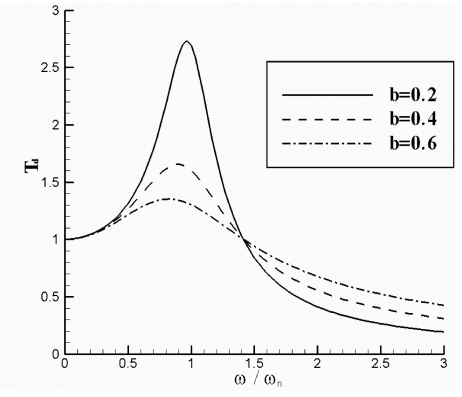

Fig. 7 The analogous problem of motion transmission from the prescribed motion point to other points (left) and the transmission ratio as a function of the frequency ratio ω/ω_n and the damping ratio b (right).

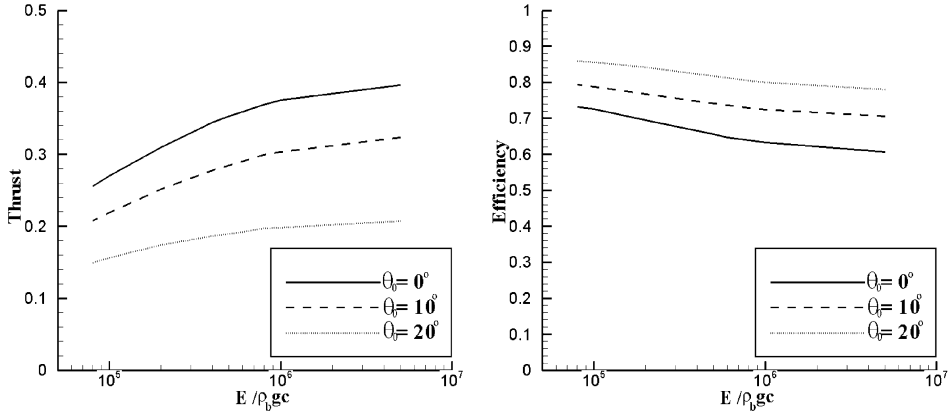

Fig. 8 Thrust coefficient (normalized by $\frac{1}{2}\rho csU^2$) and propulsion efficiency of a flapping chordwise-flexible foil in water as functions of Young's modulus.

causes the feathering of the foil. This is expected to reduce the angle of attack of the foil in relation to the upcoming flow. As illustrated in the literature, in addition to the Strouhal number, the efficiency of a rigid flapping foil is also determined by the maximum angle of attack, which is defined as

$$\alpha_m = |\theta(t) - \tan^{-1}[\dot{h}(t)/U]|_{\max} \tag{23}$$

A decreasing α_m usually leads to a decease in thrust and increase in efficiency. For example, in the cases shown in Fig. 8, considering rigid foils, $\theta_0 = (0, 10,$ and 20 deg) corresponds to $\alpha_m = (32,$ 22, and 12 deg), respectively. The thrust coefficients are 0.40, 0.32, and 0.21, and the corresponding efficiencies are 0.61, 0.71, and 0.78.

To put this in perspective, we consider a flexible foil with no pitching motion ($\theta_0 = 0$) and define an effective angle of attack as

$$\alpha_{me} = |\theta_e(t) - \tan^{-1}[\dot{h}(t)/U]|_{\max} \tag{24}$$

where $\theta_e = \tan^{-1}[(z_{\mathrm{TE}} - z_{\mathrm{LE}})/(x_{\mathrm{TE}} - x_{\mathrm{LE}})]$ is the effective pitch angle. With $E/\rho_b gc = 10^5$, we find that $\alpha_{me} \approx 23$ deg, close to the angle of attack of a rigid foil with $\theta_0 = 10$ deg. The phase of θ_e is about 90 deg behind the heave motion. Indeed, in this case, both the thrust coefficient (0.31) and the efficiency (0.73) approach the values of the rigid foil with $\theta_0 = 10$ deg and $\varphi = 90$ deg.

B. Case 2: Inertia-Driven Deformation of a Chordwise-Flexible Foil

The performance enhancement observed in case 1, however, does not appear in the inertia-driven case (Fig. 9). From the plot, it is clear that when Young's modulus is reduced, both the thrust and the efficiency plunge. For a sufficiently small Young's modulus, negative thrust (drag) is recorded. In contrast, such a sign switch has never been observed in the fluid-driven deformation case.

Similar to the fluid-driven case, the change in performance of a foil with inertia-driven deformation is also shown to be caused primarily by the change in the effective pitch angle θ_e and the effective angle of attack θ_{me}. For example, with $\theta_0 = 0$ deg and at $E/\rho_b gc = 2 \times 10^3$, θ_{me} is around 38 deg and the effective pitch lags the prescribed heave motion by an angle of 180 deg. With these kinetic parameters, similar performance decay is observed by using a rigid foil.

C. Case 3: Fluid-Driven Deformation of a Spanwise-Flexible Foil

Figure 10 shows the thrust and efficiency of a flapping foil that is able to be bent in the spanwise direction in water. It is seen that compared with a rigid foil ($E = \infty$), such a flexible foil delivers much less thrust. Interestingly, the propulsion efficiency remains somewhat unchanged throughout the whole range of E considered in our study.

The thrust diminishment is found to be the consequence of the decrease in heaving amplitude along the span of the foil. As we see in Fig. 11a, the fluid-induced deformation considerably compromises the capacity of other parts of the foil to follow the specified motion at the center. This feature leads to motion suppression close to the tips; that is, the heaving amplitude decreases along the span from the center to the tips. As a result, the average motion amplitude is smaller than that prescribed, and both the thrust generation and the energy input are reduced and the efficiency is intact.

D. Case 4: Inertia-Driven Deformation of a Spanwise-Flexible Foil

If the flapping foil is put in air (Fig. 12), it demonstrates a completely different behavior. When the stiffness of the foil is chosen to be within a special range ($10^4 < E/\rho_b gc < 10^5$), the thrust is dramatically increased (the cases in Fig. 12 show almost 100% thrust gain), whereas the efficiency is more or less unchanged. After reaching the peak, both the thrust and the efficiency plunge if the stiffness is further reduced.

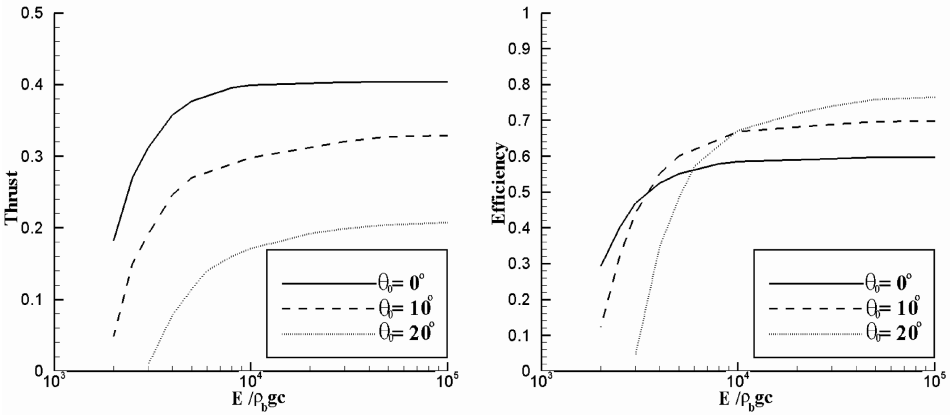

Fig. 9 Thrust coefficient (normalized by $\frac{1}{2}\rho csU^2$) and propulsion efficiency of a flapping chordwise-flexible foil in air as functions of Young's modulus.

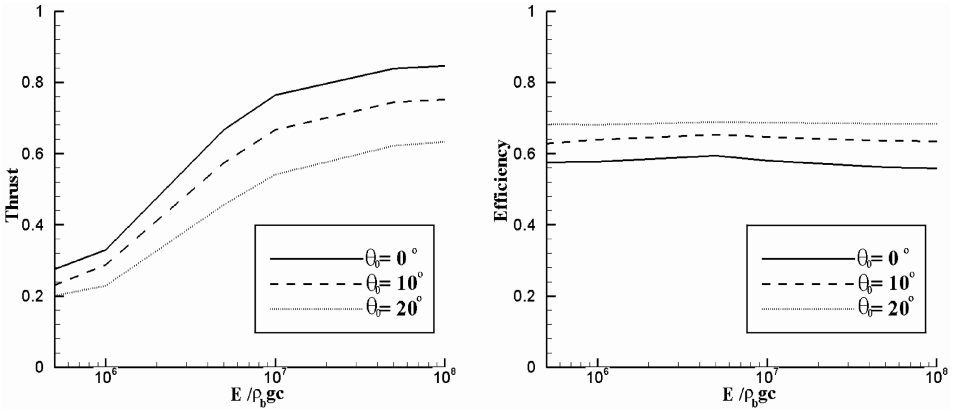

Fig. 10 Thrust coefficient (normalized by $\frac{1}{2}\rho csU^2$) and propulsion efficiency of a flapping spanwise-flexible foil in water as functions of Young's modulus.

Just as the thrust decrease in the previous case is explained by the decrease of heaving amplitude from the center of the foil to the tip, the thrust increase in the present case is the result of amplitude increasing toward the tips. As displayed in Fig. 11b, in the inertia-driven case within a certain range of foil stiffness, the tips of the foil actually overshoot the prescribed trajectory in the vicinities of the peaks and troughs along the track, indicating that it is within the amplification regime. When the stiffness of the foil is further reduced, however, we see that the system enters the motion-isolation regime and the amplitude increase along the span disappears (Fig. 11c), accompanied by the abrupt drop in thrust production, as shown in Fig. 12.

V. Conclusions

By employing a fully coupled numerical model based on the boundary-integral algorithm and the thin-plate theory, we demonstrate that the anisotropic structural flexibility of a flapping foil has significant effects on its capability of thrust generation. Moreover, the dynamics and performance of a foil bent primarily by

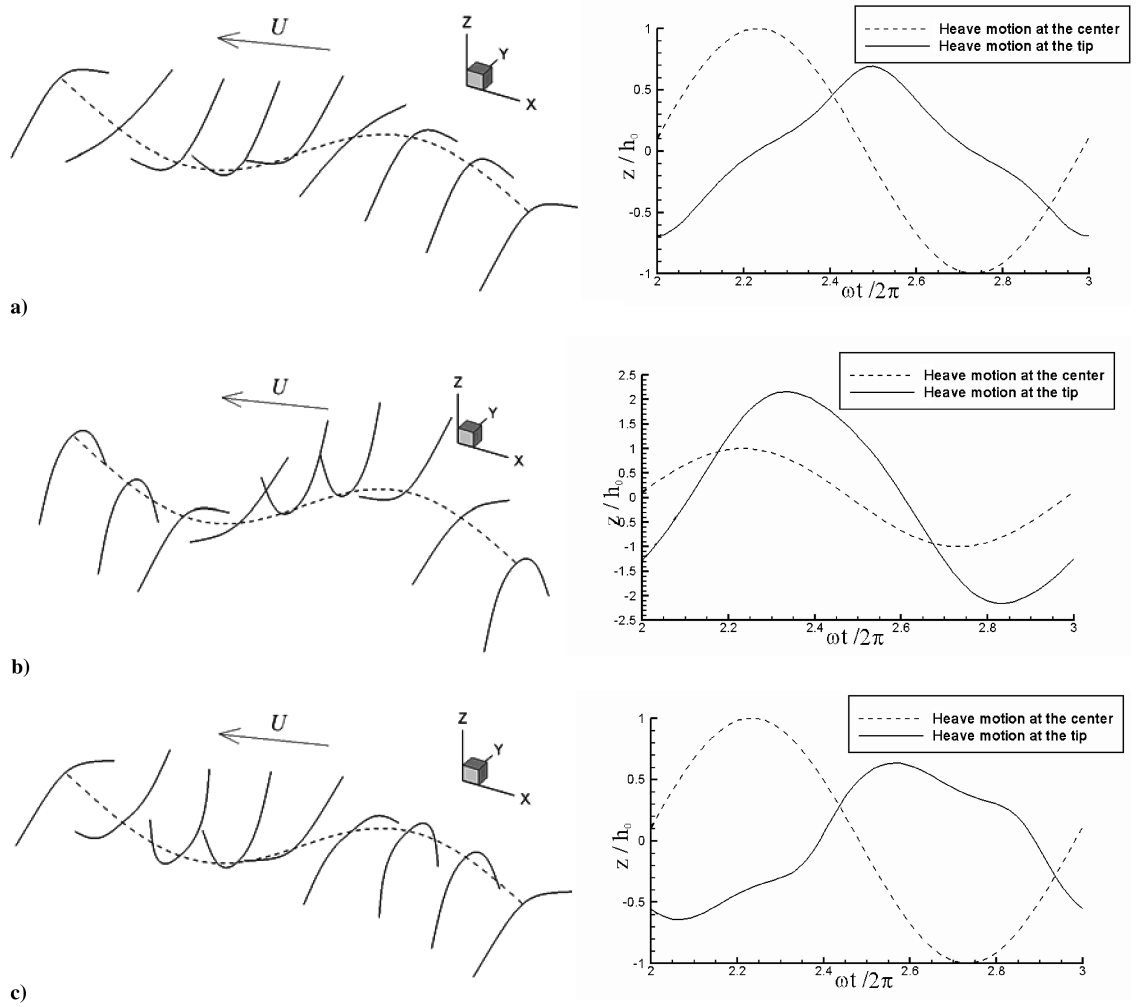

Fig. 11 Instantaneous bending of a foil with spanwise flexibility in a) water, b) air within the motion-amplification region, and c) air within the motion-isolation region; the foil undergoes heave motion only.

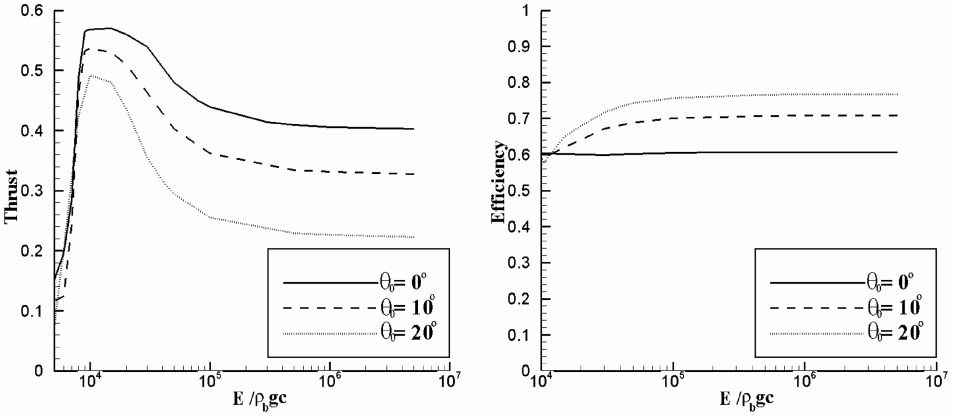

Fig. 12 Thrust coefficient (normalized by $\frac{1}{2}\rho csU^2$) and propulsion efficiency of a flapping spanwise-flexible foil in air as functions of Young's modulus.

fluid loading are shown to be utterly different from that of a foil bent by its own inertia. Among all the numerical tests we have conducted, two cases (one with chordwise flexibility and fluid-driven deformation and the other with spanwise flexibility and inertia-driven deformation) yield performance enhancement. The former shows increased efficiency and the later shows increased thrust, provided that the system lies within the motion-amplification region.

The cause of the efficiency enhancement of a chordwise-flexible foil with fluid-driven deformation is found to be the combined effect of curvature-induced thrust increase, as illustrated in previous studies [12], and the partial-feathering effect, referring to the tendency of the foil to align itself toward the tangential direction of the incoming flow. This realignment creates an additional pitching motion, for which the phase lags behind that of the heaving by an angle of approximately 90 deg. Consequently, the effective angle of attack (the angle between the flow and the instantaneous orientation of the foil, without considering the local curvature) is reduced. Although a complete feathering (i.e., when the foil is perfectly parallel to the flow) leads to zero-thrust generation and thus a reduction in propulsion efficiency, a partial feathering, as observed in our simulations, will reduce the thrust but increase the efficiency. We note that a similar effect is achievable with rigid foils by carefully choosing the amplitude of the pitching motion and its phase with respect to the heaving motion. However, to do this requires complicated control/actuation mechanisms to achieve multiple-degree-of-freedom motions. A chordwise-flexible foil therefore provides an alternative measure for highly efficient thrust generation with simple mechanical systems.

Structural flexibility may be an important mechanism for aquatic animals to improve their locomotion efficiency. In nature, the flukes of cetaceans and the fins of fishes are found to be chordwise-flexible (e.g., see Fish and Lauder [26]). On the other hand, although a chordwise-flexible fin yields high efficiency for cruising, it is achieved at the cost of thrust decease. This could be a significant disadvantage for many fish species that need the capacity of instantaneous large-thrust generation during burst swimming to catch prey or to flee from predators. This may explain why some fish species feature chordwise fin rays consisting of small pieces of cartilage (e.g., see Fish and Lauder [26], Lauder [27], and Lauder and Drucker [28]). These rays are segmented and their bending stiffness is adjustable so that the fish might be able to increase the chordwise flexibility during cruising to increase efficiency or to decease it during bursting to increase thrust production. Moreover, these rays also serve as sites of muscle attachment so that their motion can be controlled individually, enabling a fish to actively control the spanwise deformability of its caudal fin (e.g., see Fish and Lauder [26]). This actively controlled deformability is different from the passive spanwise response examined in our simulations. We have shown that spanwise flexibility attributes to significant increase in thrust without loss in efficiency. However, with purely passive deformations, the performance enhancement is only possible when the deformation is driven primarily by inertia. For a fish, this requires an extremely massive fin, which is obviously a clumsy design. Alternatively, we note that similar performance-enhancing deformations can be achieved with active control through the fin rays. Indeed, morphological evidence indicates that fish tend to bend the tips of their caudal fins toward the direction of sway [29], similar to what is shown in Fig. 11b. To understand the structure versus function of fish fins (especially the role of fin rays), additional investigations are required.

We note that the analysis in this study is based upon the potential flow framework, which is only valid in large Reynolds numbers. Thus our conclusions should not be extended to small Reynolds numbers, despite the evidence that structural flexibility may also play an important role in determining the hydrodynamic/aerodynamic performance of creatures living in the low Reynolds number regime. For example, it has been shown that insect wings display an anisotropic structure. The flexibility of these wings is determined by the architecture of embedded skeletons composed of supporting veins. By experimentally measuring and modeling the wing venation and flexural stiffness of 16 different species of insects, Combes and Daniel [7,8] confirmed that in all these species, the spanwise bending stiffness is at least one or two orders of magnitude higher than the chordwise bending stiffness. This is attributed mostly to the existence of clustered or thickened veins near the leading edge. The exact effect of this anisotropic flexibility remains a topic of further experimental investigations and low Reynolds number fluid–structure interaction modeling. Moreover, the major function of an insect's wings is to generate lift force, which is closely related to vortices created near the leading edge. A more sophisticated numerical tool is required to accurately calculate this effect. In lower Reynolds numbers, the swimming of microorganisms via flexible flagella has been investigated (e.g., see Pursell [30], Wiggins and Goldstein [31], and Becker et al. [32]); it is, however, beyond the scope of the current study.

Therefore, it is necessary to reemphasize that the paradigm applied in this study is accurate only with a limited range of Strouhal numbers, because it does not consider vorticity shedding before the trailing edge. In future investigations, it is necessary to include leading-edge separations either through special treatments to improve the accuracy of the model at high Strouhal numbers or by using unsteady Navier–Stokes simulation such as those applied by Liu and Kawachi [33], Ramamurti and Sandberg [34], or Miller and Peskin [35]. Of particular interest will be a coupled fluid–structure investigation of the 3-D viscous flow around a skeleton-reinforced biomembrane structure such as a venation–strengthened insect wing or a ray-supported fish fin.

References

[1] Lighthill, M. J., "Aquatic Animal Propulsion of High Hydrodynamical Efficiency," *Journal of Fluid Mechanics*, Vol. 44, Nov. 1970, pp. 265–301.

[2] Triantafyllou, M. S., and Triantafyllou, G. S., "An Efficient Swimming Machine," *Scientific American*, Vol. 272, No. 3, 1995, pp. 64–70.

[3] Anderson, J. M., Streitlien, K., Barret, D. S., and Triantafyllou, M. S., "Oscillating Foils for High Propulsive Efficiency," *Journal of Fluid*

Mechanics, Vol. 360, Apr. 1998, pp. 41–72.
[4] Read, D. A., "Oscillating Foils for Propulsion and Maneuvering of Ships and Underwater Vehicles," M.S. Thesis, Massachusetts Inst. of Technology, Cambridge, MA, 2000.
[5] Jones, K. D., and Platzer, M. E., "Time-Domain Analysis of Low-Speed Airfoil Flutter," *AIAA Journal*, Vol. 34, No. 5, 1996, pp. 1027–1033.
[6] Wootton, R. J., "The Mechanical Design of Insect Wings," *Scientific American*, Vol. 263, No. 5, 1990, pp. 114–120.
[7] Combes, S. A., and Daniel, T. L., "Flexible Stiffness in Insect Wings 1: Scaling and the Influence of Wing Venation," *Journal of Experimental Biology*, Vol. 206, No. 17, 2003a, pp. 2979–2987.
[8] Combes, S. A., and Daniel, T. L., "Flexible Stiffness in Insect Wings 2: Spatial Distribution and Dynamic Wing Bending," *Journal of Experimental Biology*, Vol. 206, No. 17, 2003b, pp. 2989–2997.
[9] Liao, J. C., Beal, D. N., Lauder, G. V., and Triantafyllou, M. S., "Fish Exploiting Vortices Decrease Muscle Activity," *Science*, Vol. 302, Nov. 2003, pp. 1566–1569.
[10] Zhang, J., Childress, S., Libchaber, A., and Shelley, M., "Flexible Filaments in a Flowing Soap File as a Model for One-Dimensional Flags in Two-Dimensional Wind," *Nature*, Vol. 408, Dec. 2000, pp. 835–839.
[11] Yamamoto, I., Terada, Y., Nagamatu, T., and Imaizumi, Y., "Propulsion System with Flexible Rigid Oscillating Fin," *IEEE Journal of Oceanic Engineering*, Vol. 20, No. 1, 1995, pp. 23–30.
[12] Katz, J., and Weihs, D., "Hydrodynamic Propulsion by Large Amplitude Oscillation of an Airfoil with Chordwise Flexibility," *Journal of Fluid Mechanics*, Vol. 88, No. 3, 1978, pp. 485–497.
[13] Katz, J., and Weihs, D., "Large Amplitude Unsteady Motion of a Flexible Slender Propulsor," *Journal of Fluid Mechanics*, Vol. 90, No. 4, 1979, pp. 713–723.
[14] Liu, P., and Bose, N., "Propulsive Performance from Oscillating Propulsors with Spanwise Flexibility," *Proceedings of the Royal Society of London, Series A: Mathematical and Physical Sciences*, Vol. 453, No. 1963, 1997, pp. 1763–1770.
[15] Daniel, T. L., and Combes, S. A., "Flexible Wings and Fins: Bending by Inertial or Fluid-Dynamic Forces?," *Integrative and Comparative Biology*, Vol. 42, No. 5, 2002, pp. 1044–1049.
[16] Doyle, J. F., *Nonlinear Analysis of Thin-Walled Structures*, Springer–Verlag, New York, 2001.
[17] Zhu, Q., Wolfgang, M., Yue, D. K. P., and Triantafyllou, M. S., "Three-Dimensional Flow Structures and Vorticity Control in Fish-Like Swimming," *Journal of Fluid Mechanics*, Vol. 468, Oct. 2002, pp. 1–28.
[18] Wolfgang, M., Anderson, J., Grosenbaugh, M., Yue, D. K. P., and Triantafyllou, M. S., "Near-Body Flow Dynamics in Swimming Fish," *Journal of Experimental Biology*, Vol. 202, No. 17, 1999, pp. 2303–2327.
[19] Kinnas, S. A., and Hsin, C.-Y., "A Boundary Element Method for the Analysis of the Unsteady Flow Around Extreme Propeller Geometries," *AIAA Journal*, Vol. 30, No. 3, 1992, pp. 688–696.
[20] Zhu, Q., Liu, Y., and Yue, D. K. P., "Dynamics of a Three-Dimensional Oscillating Foil Near the Free Surface," *AIAA Journal*, Vol. 44, No. 2, 2006, pp. 2997–3009.
[21] Katz, J., and Plotkin, A., *Low-Speed Aerodynamics: From Wing Theory to Panel Methods*, McGraw–Hill, New York, 1991.
[22] Krasny, R., "Desingularization of Periodic Vortex Sheet Roll-Up," *Journal of Computational Physics*, Vol. 65, No. 2, 1986, pp. 292–313.
[23] Tuncer, I. H., and Platzer, M. F., "Thrust Generation Due to Airfoil Flapping," *AIAA Journal*, Vol. 34, No. 2, 1996, pp. 324–331.
[24] Heathcote, S., Martin, D., and Gursul, I., "Flexible Flapping Airfoil Propulsion at Zero Freestream Velocity," *AIAA Journal*, Vol. 42, No. 11, 2004, pp. 2196–2204.
[25] Triantafyllou, M. S., Triantafyllou, G. S., and Grosenbaugh, M., "Optimal Thrust Development in Oscillating Foils with Application to Fish Propulsion," *Journal of Fluids and Structures*, Vol. 7, No. 2, 1993, pp. 205–224.
[26] Fish, F. E., and Lauder, G. V., "Passive and Active Flow Control by Swimming Fishes and Mammals," *Annual Review of Fluid Mechanics*, Vol. 38, 2006, pp. 193–224.
[27] Lauder, G. V., "Caudal fin Locomotion in Ray-Finned Fishes: Historical and Functional Analyses," *American Zoologist*, No. 1, Vol. 29, 1989, pp. 85–102.
[28] Lauder, G. V., and Drucker, E. G., "Morphology and Experimental Hydrodynamics of Fish Fin Control Surfaces," *IEEE Journal of Oceanic Engineering*, Vol. 29, No. 3, 2004, pp. 556–571.
[29] Videler, J. J., *Fish Swimming*, Chapman & Hall, Boca Raton, FL, 1993.
[30] Purcell, E. M., "The Efficiency of Propulsion by a Rotating Flagellum," *Proceedings of the National Academy of Sciences of the United States of America*, Vol. 94, No. 21, 1997, pp. 11,307–11,311.
[31] Wiggins, C. H., and Goldstein, R. E., "Flexive and Propulsive Dynamics of Elastica at Low Reynolds Number," *Physical Review Letters*, Vol. 80, No. 17, 1998, pp. 3879–3882.
[32] Becker, L. E., Koehler, S. A., and Stone, H. A., "On Self-Propulsion of Micro-Machines at Low Reynolds Number: Purcell's Three-Link Swimmer," *Journal of Fluid Mechanics*, Vol. 490, Sept. 2003, pp. 15–35.
[33] Liu, H., and Kawachi, K., "A Numerical Study of Insect Flight," *Journal of Computational Physics*, Vol. 146, No. 1, 1998, pp. 124–156.
[34] Ramamurti, R., and Sandberg, W. C., "A Three-Dimensional Computational Study of the Aerodynamic Mechanisms of Insect Flight," *Journal of Experimental Biology*, Vol. 205, No. 10, 2002, pp. 1507–1518.
[35] Miller, L. A., and Peskin, C. S., "When Vortices Stick: An Aerodynamic Transition in Tiny Insect Flight," *Journal of Experimental Biology*, Vol. 207, No. 17, 2004, pp. 3073–3088.

A. Plotkin
Associate Editor